actuators

MDPI

Article

Design of a Suspension Controller with Human Body Model for Ride Comfort Improvement and Motion Sickness Mitigation

Jinwoo Kim and Seongjin Yim *

Department of Mechanical and Automotive Engineering, Seoul National University of Science and Technology, 232 Gongneung-ro, Nowon-gu, Seoul 01811, Republic of Korea; king@g.seoultech.ac.kr
* Correspondence: acebtif@seoultech.ac.kr; Tel.: +82-2-970-9011

Abstract: This paper presents a method to design a suspension controller with a human body model for ride comfort improvement and motion sickness mitigation. Generally, it has been known that the vertical acceleration of a sprung mass should be reduced for ride comfort. On the other hand, recent studies have shown that, combined, the vertical acceleration and pitch rate of a sprung mass are key factors that cause motion sickness. However, those variables have been considered with respect to the center of gravity of a sprung mass. For motion sickness mitigation, the vertical acceleration of a human head should be also considered. In this paper, the vertical accelerations and pitch rates of a sprung mass and a human head are controlled by a suspension controller for ride comfort improvement and motion sickness mitigation. For the controller design, a half-car and human body models are adopted. With those models, several types of static output feedback suspension controller are designed with linear quadratic optimal control methodology. To reduce the pitch rate of the sprung mass and the vertical acceleration of the head, a filtered-X LMS algorithm is adopted as an adaptive feedforward algorithm and combined with the static output feedback controllers. A frequency response analysis and simulation are performed with the designed controllers on vehicle simulation software, CarSim®. From the simulation results, it is shown that the proposed controllers can effectively reduce the vertical accelerations and the pitch rate of the sprung mass and the human head.

Keywords: autonomous driving; ride comfort; motion sickness; human body model; active suspension control; adaptive feedforward algorithm

check for updates

Citation: Kim, J.; Yim, S. Design of a Suspension Controller with Human Body Model for Ride Comfort Improvement and Motion Sickness Mitigation. *Actuators* **2024**, *13*, 520. https://doi.org/10.3390/act13120520

Academic Editor: Norman M. Wereley

Received: 23 October 2024
Revised: 11 December 2024
Accepted: 14 December 2024
Published: 16 December 2024

Copyright: © 2024 by the authors. Licensee MDPI, Basel, Switzerland. This article is an open access article distributed under the terms and conditions of the Creative Commons Attribution (CC BY) license (https://creativecommons.org/licenses/by/4.0/).

1. Introduction

To date, a suspension controller has been designed to improve ride comfort and road handling [1–3]. Generally, it has been well known that the vertical acceleration of a sprung mass and tire deflection are regarded as a measure for ride comfort and road holding [1]. Ride comfort was specified within ISO2631-1, which represents the sensitivity of the human body to vibration [4]. According to ISO2631-1, the vertical acceleration of a sprung mass (SPM) within the range of 4~10 Hz should be reduced for ride comfort. On the other hand, vertical acceleration of an SPM ($a_{z,\mathrm{SPM}}$) over the frequency range from 0.1 to 0.2 Hz should be reduced for motion sickness. However, ISO2631-1 originated from the analysis of the vibration on a ship.

Autonomous driving can make passengers concentrate on non-driving tasks, such as reading a display device or a book in a car. However, this can make motion sickness severe [5,6]. Recent studies have shown that the pitch rate of an SPM ($\omega_{y,\mathrm{SPM}}$) is also important for motion sickness and that the combination ($a_{z,\mathrm{SPM}}$ and $\omega_{y,\mathrm{SPM}}$) can cause motion sickness within the frequency band of 0.8~8 Hz when reading a book in a car [7,8]. Fortunately, this frequency band is overlapped with that for ride comfort, given from ISO2631-1. For this reason, it is necessary to reduce $a_{z,\mathrm{SPM}}$ and $\omega_{y,\mathrm{SPM}}$ for the purpose of improving ride comfort and mitigating motion sickness. For this purpose, a suspension controller is designed in this paper.

To date, there have been few studies on motion sickness on passengers in a car. Among them, studies concentrating on suspension control were even rarer [7–9]. Recent studies on active suspension control for motion sickness mitigation have concentrated on controller design with active suspension [10–12]. Following those studies, this paper presents a method to design an active suspension controller for motion sickness mitigation.

The methods proposed to date for active suspension control have used quarter-, half- and full-car models [1]. However, those studies did not consider a human body model (HBM) in the controller design stage because the goal of suspension control is to improve the ride comfort or road handling of a vehicle body or an SPM. According to a survey, there are a lot of HBMs that have been used for analyzing the vertical vibration of a human body [13]. The frequency responses and eigen frequencies were analyzed in the reference. To date, a half-car model (HCM), describing the vertical and pitch motions of an SPM, and a human body model (HBM), describing the vertical motion of a head and an abdomen in a human body, have been adopted for suspension controller design [14–17]. In an HBM, the vertical acceleration of a head ($a_{z,\mathrm{HEAD}}$) is the most important measure. Among them, this paper selects the most relevant model describing $a_{z,\mathrm{HEAD}}$ as an HBM for controller design [18]. Following those papers, this paper adopts an HCM and its combination with an HBM for motion sickness mitigation. Moreover, the model parameters are referred from [18], which have been used in the previous work [14–17].

Generally, a full-state feedback controller for suspension control is hard to implement on a real vehicle because it requires all state variables to be exactly measured or estimated and it has so many gain elements. To overcome the problems, this paper selects a static output feedback (SOF) control as the controller structure [10–12,19–22]. Based on the geometric relationship between front and rear suspensions along the pitch motion of an SPM, this paper presents three types of structured SOF controllers. As an output for the SOF control, this paper selects six variables, i.e., the vertical velocity of the SPM ($v_{z,\mathrm{SPM}}$) and $\omega_{y,\mathrm{SPM}}$, the vertical velocities at the front/rear corners of an SPM ($v_{z,\mathrm{SPMFC}}$ and $v_{z,\mathrm{SPMRC}}$) and the suspension velocities at the front/rear suspensions ($v_{z,\mathrm{SSF}}$ and $v_{z,\mathrm{SSR}}$). To optimize those SOF controllers in view of ride comfort enhancement and motion sickness mitigation, this paper adopts linear quadratic optimal control (LQOC) [10–12]. As a result, linear quadratic SOF (LQ SOF) controllers are obtained.

To improve the performance of SOF controllers, this paper adopts a wheelbase preview scheme, which uses signals obtained from the front suspensions and generates a control force at the rear suspensions [23–26]. Figure 1 shows the wheelbase preview control scheme. For the structure of the wheelbase preview scheme, there are delays between the front and rear wheels or suspension. Under the situation, it is natural to use a feedforward controller in view of an actuator located at the rear suspensions. This paper selects a filtered-x LMS (FxLMS) algorithm as an adaptive feedforward controller, which tries to reduce the $\omega_{y,\mathrm{SPM}}$ [12,27,28]. The FxLMS algorithm is combined with the LQ SOF controller for ride comfort improvement and motion sickness mitigation.

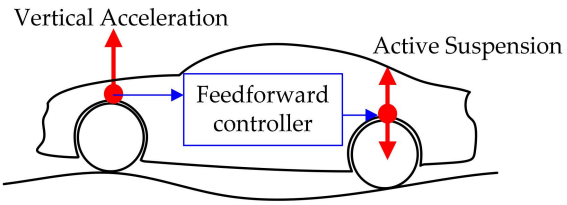


Figure 1. Wheelbase preview control scheme.

To validate the LQ SOF controllers combined with the FxLMS algorithm, a frequency response analysis is performed with a state-space equation and a simulation is conducted on a vehicle simulation package. From the simulation results, it is concluded which type of SOF controller and its combination with an FxLMS is relevant for motion sickness mitigation.

The goal of this paper is to design LQ SOF controllers and the FxLMS algorithm with an HCM and HBM for motion sickness reduction. The contributions of this paper can be summarized as follows:

1. Several types of LQ SOF controllers are designed to reduce the $a_{z,\mathrm{SPM}}$, $\omega_{y,\mathrm{SPM}}$ and $a_{z,\mathrm{HEAD}}$ over the frequency range from 0.8 to 8.0 Hz. With the outputs, $v_{z,\mathrm{SPM}}$, $\omega_{y,\mathrm{SPM}}$, $v_{z,\mathrm{SPMFC}}$, $v_{z,\mathrm{SPMRC}}$, $v_{z,\mathrm{SSF}}$ and $v_{z,\mathrm{SSR}}$, four LQ SOF controllers are proposed.
2. To reduce the $\omega_{y,\mathrm{SPM}}$ over the frequency range from 0.8 to 8.0 Hz, an FxLMS algorithm is applied in the framework of the wheelbase preview control scheme.
3. With the LQ SOF controllers and FxLMS algorithm, a simulation is performed on CarSim. Through the simulation, it is shown which LQ SOF controller is better for ride comfort enhancement and whether the FxLMS is effective or not for motion sickness reduction.

This paper consists of five sections. An HMC and HBM are presented, and its state-space models are derived in Section 2. With the state-space model, three SOF controllers are proposed and LQ SOF controllers are designed with the LQOC methodology. The FxLMS is designed in Section 2. In Section 3, a simulation with LQ SOF controllers and the FxLMS is performed on CarSim and the simulation results are analyzed and discussed. The conclusions are drawn in Section 4.

2. Controller Design for Motion Sickness Mitigation

In this section, the state-space models are derived from an HCM and a combined HCM-HBM, as presented in the previous studies [10–12,18]. With the state-space models and LQ cost functions set for ride comfort enhancement and motion sickness mitigation, four types of LQ SOF controllers are proposed and designed with LQOC. In order to reduce $\omega_{y,\mathrm{SPM}}$, the FxLMS algorithm is designed and applied.

2.1. Half-Car and Human Body Models

Figures 2 and 3 show the HCM and the HBM [10–12,18]. The HBM given in Figure 3 can be found in the references [14–18]. As shown in Figure 2, there is a single SPM and two unsprung masses (USPMs). Front and rear suspensions, S_f and S_r, are between the SPM and USPMs, which consist of a spring, k_s, and a damper, b_s, and an active actuator used to generate control vertical forces, u_f and u_r. The HCM describes the vertical and pitch motions of the SPM and the vertical motions of the USPMs. In Figure 2, A_{sf}, A_{sr}, A_{uf} and A_{ur} are the accelerometers, installed on the front/rear corners of the SPM (SPMFC and SPMRC) and the wheel centers of the USPMs, respectively. These accelerometers are used to measure the vertical acceleration of the SPMFC, SPMRC and front/rear USPMs, which are denoted as $a_{z,\mathrm{SPMFC}}$, $a_{z,\mathrm{SPMRC}}$, $a_{z,\mathrm{USPMF}}$ and $a_{z,\mathrm{USPMR}}$, respectively. There are four equations of motions in the HCM [10–12].

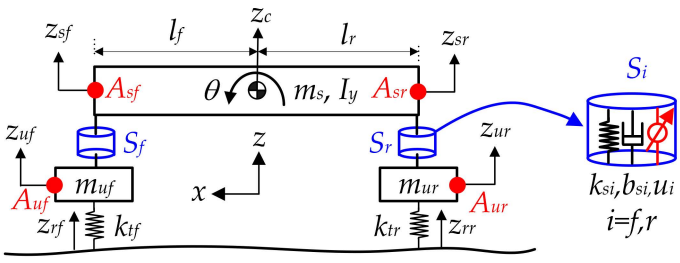


Figure 2. Half-car model.

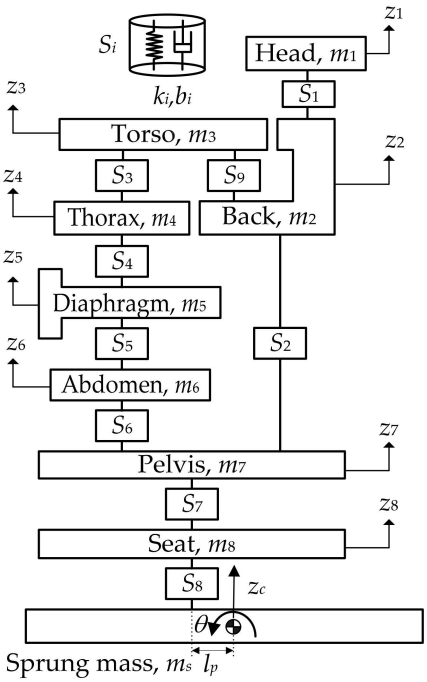


Figure 3. Human body model with the seat, connected to the sprung mass [14–18].

As shown in Figure 3, the HBM has eight masses, $m_1, \ldots, m_8$, and eight suspensions, $S_1, \ldots, S_8$. The seat is connected to the SPM of the HCM through S_8. In the HBM, each S_i has a spring, k_i, and a damper, b_i. As shown in Figure 3, there is the offset l_p between the centers of gravity of the SPM and the seat. Due to this offset, $\omega_{y,\mathrm{SPM}}$ has an effect on the vertical motions of the human body [18]. In the HBM, the most important dynamic variable is the vertical acceleration of m_1, i.e., $a_{z,\mathrm{HEAD}}$. For motion sickness mitigation, this should be reduced by a controller. There are eight equations of motions in the HBM [14–18].

This paper combines the HCM and HBM into a single model, which is denoted as HCHBM. The HCHBM has twelve equations of motions because HCM and HBM have four and eight equations of motions, respectively. Among them, the vertical and pitch motions of the SPM, and the vertical motions of the head and the abdomen in a human body are important in view of motion sickness.

In the HCM, using the geometric relationship of the SPM, the vertical displacements at SPMFC and SPMRC are obtained as (1). Using the approximation, $\sin\theta \approx \theta$, z_{sf} and z_{sr} are calculated as (1) from z_c and θ of the SPM. Equation (1) is converted into (2). New vectors and a matrix are defined as (3). The vectors of disturbances and control inputs, $\mathbf{w}$ and $\mathbf{u}$, are defined in (3). With those definitions in (3), (2) is converted into (4). The time-derivative of (4) and its inverse are obtained as (5). In (5), $\mathbf{X}^+$ stands for a pseudo-inverse of a matrix, $\mathbf{X}$. Equation (5) represents the relationship between $v_{z,\mathrm{SPM}}$ and $\omega_{y,\mathrm{SPM}}$ and $v_{z,\mathrm{SPMFC}}$ and $v_{z,\mathrm{SPMRC}}$. With (5), $v_{z,\mathrm{SPM}}$ and $\omega_{y,\mathrm{SPM}}$ are calculated from $v_{z,\mathrm{SPMFC}}$ and $v_{z,\mathrm{SPMRC}}$. For the reason, $v_{z,\mathrm{SPM}}$ and $\omega_{y,\mathrm{SPM}}$ play an identical role to $v_{z,\mathrm{SPMFC}}$ and $v_{z,\mathrm{SPMRC}}$ in controller.

$$\begin{cases} z_{sf} = z_c - l_f \sin\theta \simeq z_c - l_f\theta \\ z_{sr} = z_c + l_r \sin\theta \simeq z_c + l_r\theta \end{cases} \tag{1}$$

$$\begin{bmatrix} z_{sf} \\ z_{sr} \end{bmatrix} = \begin{bmatrix} 1 & -l_f \\ 1 & l_r \end{bmatrix} \begin{bmatrix} z_c \\ \theta \end{bmatrix} \tag{2}$$

$$\mathbf{p} \triangleq \begin{bmatrix} z_c \\ \theta \end{bmatrix},\ \mathbf{z}_s \triangleq \begin{bmatrix} z_{sf} \\ z_{sr} \end{bmatrix},\ \mathbf{z}_u \triangleq \begin{bmatrix} z_{uf} \\ z_{ur} \end{bmatrix},\ \mathbf{w} = \mathbf{z}_r \triangleq \begin{bmatrix} z_{rf} \\ z_{ru} \end{bmatrix},\ \mathbf{u} \triangleq \begin{bmatrix} u_f \\ u_r \end{bmatrix},\ \mathbf{G} \triangleq \begin{bmatrix} 1 & 1 \\ -l_f & l_r \end{bmatrix} \tag{3}$$

$$\mathbf{z}_s = \mathbf{G}^T \mathbf{p} \tag{4}$$

$$\dot{\mathbf{z}}_s = \mathbf{G}^T \dot{\mathbf{p}} \;\Leftrightarrow\; \dot{\mathbf{p}} = \left(\mathbf{G}^T\right)^+ \dot{\mathbf{z}}_s \tag{5}$$

For HCM and HBM, the state vectors, $\mathbf{z}_H$ and $\mathbf{z}_B$, are defined as (6). In (6), the subscript H and B stand for HCM and HBM, respectively. If the state vector of HCM, $\mathbf{x}_H$, is defined as (7), the state-space equation for the HCM is derived as (8) [10–12]. If the state vector of HCHBM, $\mathbf{x}_F$, is defined as (9), the state-space equation for HCHBM is derived as (10) [14–18]. In (8) and (10), the subscripts, H and F, represent HCM and HCHBM, respectively. As shown in (7) and (9), the state-space equations for HCM and HCHBM have 8 and 24 state variables, respectively. It should be noted that the disturbance, $\mathbf{w}$, and the control input, $\mathbf{u}$, in HCM and HCHBM are identical, as given in (3). The detailed derivation of (8) and (10) can be found in the reference [10–12,14–18].

$$\begin{cases} \mathbf{z}_H \triangleq \begin{bmatrix} \mathbf{p} \\ \mathbf{z}_u \end{bmatrix} \\ \mathbf{z}_B \triangleq \begin{bmatrix} z_1 & z_2 & z_3 & z_4 & z_5 & z_6 & z_7 & z_8 \end{bmatrix}^T \end{cases} \tag{6}$$

$$\mathbf{x}_H \triangleq \begin{bmatrix} \mathbf{z}_H^T & \dot{\mathbf{z}}_H^T \end{bmatrix}^T \tag{7}$$

$$\dot{\mathbf{x}}_H = \mathbf{A}_H \mathbf{x}_H + \mathbf{B}_{1H} \mathbf{w} + \mathbf{B}_{2H} \mathbf{u} \tag{8}$$

$$\mathbf{x}_F \triangleq \begin{bmatrix} \mathbf{z}_B^T & \mathbf{z}_H^T & \dot{\mathbf{z}}_B^T & \dot{\mathbf{z}}_H^T \end{bmatrix}^T \tag{9}$$

$$\dot{\mathbf{x}}_F = \mathbf{A}_F \mathbf{x}_F + \mathbf{B}_{1F} \mathbf{w} + \mathbf{B}_{2F} \mathbf{u} \tag{10}$$

2.2. Design of SOF Controllers with Linear Quadratic Optimal Control

Typical method used to suspension controller design is LQR, which is a feedback controller. There are two LQRs for the HCM and HCHBM: LQRH and LQRF. For designing LQRH and LQRF with (8) and (10), the corresponding LQ cost functions are defined as (11) and (12), respectively [10–12,14–18]. As given in (12), the difference between J_H and J_F is that J_F has the term on $a_{z,\mathrm{HEAD}}$. In (11) and (12), the weight ρ_i is determined by Bryson's rule, (13), where ζ_i is the maximum allowable value (MAV) of each term [29].

$$\begin{aligned} J_H &= \int_0^\infty \left\{ \begin{array}{c} \rho_1 \ddot{z}_c^2 + \rho_2 \ddot{\theta}^2 + \rho_3 \dot{\theta}^2 + \rho_4 \theta^2 \\ +\rho_5 \sum_{i=f,r} (z_{si} - z_{ui})^2 + \rho_6 \sum_{i=f,r} z_{ui}^2 + \rho_7 \sum_{i=f,r} u_i^2 \end{array} \right\} dt \\ &= \int_0^\infty \left\{ \begin{bmatrix} \mathbf{x}_H \\ \mathbf{u} \end{bmatrix}^T \begin{bmatrix} \mathbf{Q}_H & \mathbf{N}_H \\ \mathbf{N}_H^T & \mathbf{R}_H \end{bmatrix} \begin{bmatrix} \mathbf{x}_H \\ \mathbf{u} \end{bmatrix} \right\} dt \end{aligned} \tag{11}$$

$$J_F = J_H + \int_0^\infty \rho_8 \ddot{z}_1^2 dt = \int_0^\infty \left\{ \begin{bmatrix} \mathbf{x}_F \\ \mathbf{u} \end{bmatrix}^T \begin{bmatrix} \mathbf{Q}_F & \mathbf{N}_F \\ \mathbf{N}_F^T & \mathbf{R}_F \end{bmatrix} \begin{bmatrix} \mathbf{x}_F \\ \mathbf{u} \end{bmatrix} \right\} dt \tag{12}$$

$$\rho_i = \frac{1}{\zeta_i^2},\ i = 1, 2, \cdots, 8 \tag{13}$$

For ride comfort improvement and motion sickness mitigation, ζ_1 and ζ_3 in J_H and ζ_1, ζ_3 and ζ_8 in J_F should be set smaller while maintaining other terms as constant. Using the matrices, $\mathbf{Q}$, $\mathbf{R}$ and $\mathbf{N}$ obtained in (11) and (12), the gain matrices of LQRH and LQRF are obtained as $\mathbf{K}_{LQRH}$ and $\mathbf{K}_{LQRF}$, as given in (14), respectively. In (14), $\mathbf{P}_H$ and $\mathbf{P}_F$ are the

solutions of Riccati equations, corresponding to (8) and (10), respectively. As mentioned earlier, regardless of J_H and J_F, the disturbance, $\mathbf{w}$, and the control input, $\mathbf{u}$, in J_H and J_F.

As shown in (3), (8) and (10), the number of state variables and control inputs in $\mathbf{x}_F$ and $\mathbf{u}$ are 24 and 2, respectively. Hence, the gain matrix of LQRF, i.e., $\mathbf{K}_{LQRF}$, has the dimension of 2×24, which is too large for $\mathbf{K}_{LQRF}$ to be implemented on a real vehicle. Especially, it is very difficult to measure all the state variables of $\mathbf{z}_B$ in the HBM. To overcome the problem, this paper selects a SOF control as a controller structure.

$$\begin{cases} \mathbf{u} = -\mathbf{K}_{LQRH}\mathbf{x}_H = -\mathbf{R}_H^{-1}\mathbf{B}_{2H}^T\mathbf{P}_H\mathbf{x}_H \\ \mathbf{u} = -\mathbf{K}_{LQRF}\mathbf{x}_F = -\mathbf{R}_F^{-1}\mathbf{B}_{2F}^T\mathbf{P}_F\mathbf{x}_F \end{cases} \tag{14}$$

This paper selects six signals, $v_{z,\mathrm{SPM}}$, $\omega_{y,\mathrm{SPM}}$, $v_{z,\mathrm{SPMFC}}$, $v_{z,\mathrm{SPMRC}}$, $v_{z,\mathrm{SSF}}$ and $v_{z,\mathrm{SSR}}$, as the sensor outputs for the SOF control, as given in (15) [8]. It is relatively easy to measure those signals in a real vehicle. Moreover, the output vector, $\mathbf{y}$, has no state variables of $\mathbf{z}_B$ to be measured from the HBM. Hence, $\mathbf{y}$ can be derived from $\mathbf{x}_H$ and $\mathbf{x}_B$, as given in (15).

$$\mathbf{y} \triangleq \begin{bmatrix} \dot{z}_c \\ \dot{\theta} \\ \dot{z}_{sf} - \dot{z}_{uf} \\ \dot{z}_{sr} - \dot{z}_{ur} \\ \dot{z}_{sf} \\ \dot{z}_{sr} \end{bmatrix} = \begin{bmatrix} v_{z,SPM} \\ \omega_{z,SPM} \\ v_{z,SSF} \\ v_{z,SSR} \\ v_{z,SPMFC} \\ v_{z,SPMRC} \end{bmatrix} = \begin{cases} \mathbf{C}_H\mathbf{x}_H = \begin{bmatrix} \mathbf{0}_{6\times 4} & \mathbf{C}_X \end{bmatrix}\mathbf{x}_H \\ \mathbf{C}_F\mathbf{x}_F = \begin{bmatrix} \mathbf{0}_{6\times 20} & \mathbf{C}_X \end{bmatrix}\mathbf{x}_F \end{cases}, \quad \mathbf{C}_X \triangleq \begin{bmatrix} 1 & 0 & 0 & 0 \\ 0 & 1 & 0 & 0 \\ 1 & -l_f & -1 & 0 \\ 1 & l_r & 0 & -1 \\ 1 & -l_f & 0 & 0 \\ 1 & l_r & 0 & 0 \end{bmatrix} \tag{15}$$

The sensor output signals in $\mathbf{y}$ can be obtained by filtering and integrating the acceleration signals measured from four accelerometers, A_{sf}, A_{sr}, A_{uf} and A_{ur}, in the SPM and USPMs as given in Figure 2. As shown in Figure 4, the signals measured from four accelerometers are filtered sequentially through a high-pass filter (HPF) and low-pass filter (LPF) for the purpose of noise cancellation and DC blocking, respectively. The details of the HPF and LPF can be found in the references [11,30–32].

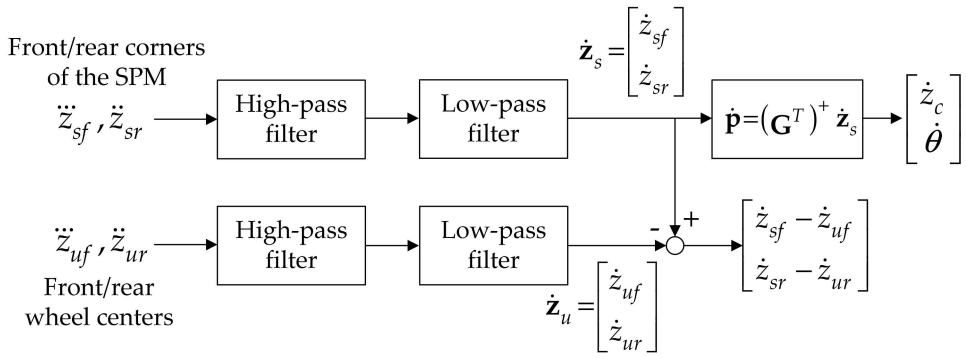


Figure 4. Block diagram on calculation procedure of velocity and angular rate from acceleration signals.

With these signals, four types of SOF controller were proposed as (16), (17), (18) and (19) in the previous work. In (16), $\mathbf{u}_{SOF}$ is a standard form of SOF controller with two control inputs and six output signals given in (15). On the other hand, there is the geometric relationship between the pitch motion of the SPM and vertical motions of SPMFC and SPMRC, as given in (4) and (5). Using this fact, $\mathbf{u}_{SSOF1}$ and $\mathbf{u}_{SSOF2}$ can be set as (17) and (18), respectively. In (18), $\mathbf{u}_{SSOF2}$ is derived from the fact that u_f and u_r are calculated from $v_{z,\mathrm{SPM}}$ and $\omega_{y,\mathrm{SPM}}$. As shown in (17) and (18), $\mathbf{u}_{SSOF1}$ and $\mathbf{u}_{SSOF2}$ use four and two output signals in $\mathbf{y}$, respectively. In (19), $\mathbf{u}_{SSOF3}$ is derived from the fact that u_f and u_r are calculated from $v_{z,\mathrm{SPMFC}}$ and $v_{z,\mathrm{SPMRC}}$, respectively. As shown in (19), $\mathbf{u}_{SSOF3}$ uses only two output signals

in $\mathbf{y}$. In $\mathbf{u}_{SSOF1}$, $\mathbf{u}_{SSOF2}$ and $\mathbf{u}_{SSOF3}$, the subscript SSOF represents a structured SOF (SSOF) because the gain matrices, $\mathbf{K}_{SSOF1}$, $\mathbf{K}_{SSOF2}$ and $\mathbf{K}_{SSOF3}$, are structured in a particular way.

$$\mathbf{u}_{SOF} = \mathbf{K}_{SOF}\mathbf{y} = \begin{bmatrix} k_1 & k_2 & k_3 & k_4 & k_5 & k_6 \\ k_7 & k_8 & k_9 & k_{10} & k_{11} & k_{12} \end{bmatrix}\mathbf{y} \tag{16}$$

$$\mathbf{u}_{SSOF1} = \mathbf{K}_{SSOF1}\mathbf{y} = \begin{bmatrix} k_1 & k_2 & k_3 & 0 & 0 & 0 \\ k_1 & -k_2 & 0 & k_3 & 0 & 0 \end{bmatrix}\mathbf{y} \tag{17}$$

$$\mathbf{u}_{SSOF2} = \mathbf{K}_{SSOF2}\mathbf{y} = \begin{bmatrix} k_1 & k_2 & 0 & 0 & 0 & 0 \\ k_1 & -k_2 & 0 & 0 & 0 & 0 \end{bmatrix}\mathbf{y} \tag{18}$$

$$\mathbf{u}_{SSOF3} = \mathbf{K}_{SSOF3}\mathbf{y} = \begin{bmatrix} 0 & 0 & 0 & 0 & k_1 & k_2 \\ 0 & 0 & 0 & 0 & k_2 & k_1 \end{bmatrix}\mathbf{y} \tag{19}$$

To find an optimal gain matrix of the SOF controllers, the optimization problem is formulated as (20). In (20), $\mathbf{K}_s$ is either $\mathbf{K}_{SOF}$ or $\mathbf{K}_{SSOF1}$ or $\mathbf{K}_{SSOF2}$ or $\mathbf{K}_{SSOF3}$. The subscript q is one of H and F, which represent (7) and (9), respectively. The second row of the constraints in (20) means that the closed-loop system should be stable. This means that the state-space equations, (8) and (10), can be used for designing the SOF controllers. If is designed with the HCM, then the subscript q is H, and (8) and (11) are needed for controller design. If is designed with the HCHBM, then the subscript q is F, and (10) and (12) are needed for controller design.

$$\begin{aligned} &\min_{\mathbf{K}_S} J_{SOF} = \operatorname{trace}(\mathbf{P}_q) \\ &s.t. \begin{cases} \mathbf{P}_q = \mathbf{P}_q^T > 0 \\ \max\left(\operatorname{Re}\left[\mathbf{A}_q + \mathbf{B}_{2q}\mathbf{K}_S\mathbf{C}_q\right]\right) < 0 \\ \left(\mathbf{A}_q + \mathbf{B}_{2q}\mathbf{K}_S\mathbf{C}_q\right)^T\mathbf{P}_q + \mathbf{P}_q\left(\mathbf{A}_q + \mathbf{B}_{2q}\mathbf{K}_S\mathbf{C}_q\right) \\ \qquad +\mathbf{Q}+\mathbf{C}_q^T\mathbf{K}_S^T\mathbf{N}_q^T + \mathbf{N}_q\mathbf{K}_S\mathbf{C}_q + \mathbf{C}_q^T\mathbf{K}_S^T\mathbf{R}_q\mathbf{K}_S\mathbf{C}_q = 0 \end{cases} \end{aligned} \tag{20}$$

For optimization, this paper uses a heuristic optimization method, CMS-ES [33,34]. Let denote the resulting SSOF controllers from (20) as a LQ SSOF controller.

Let denote the SOF controllers, $\mathbf{K}_{SOF}$, $\mathbf{K}_{SSOF1}$, $\mathbf{K}_{SSOF2}$ and $\mathbf{K}_{SSOF3}$, designed with (8) and (11) as LQSOFH, LQSSOFH1, LQSSOFH2 and LQSSOFH3, respectively. Let denote the group of these LQ SOF controllers as LQSOF.HCM. Let denote the SOF controllers, $\mathbf{K}_{SOF}$, $\mathbf{K}_{SSOF1}$, $\mathbf{K}_{SSOF2}$ and $\mathbf{K}_{SSOF3}$, designed with (10) and (12) as LQSOFF, LQSSOFF1, LQSSOFF2 and LQSSOFF3, respectively. Let denote the group of these LQ SOF controllers as LQSOF.HCHBM. Those SOF and SSOF controllers are compared with one another in terms of ride comfort and motion sickness through simulation on CarSim.

2.3. Design of Adaptive Feedforward Controller with Filtered-X LMS Algorithm

The FxLMS has been applied to systems with delays from a reference signal to a control input. A typical example is active noise control (ANC) and suspension control with a wheelbase preview control scheme [35–43]. Based on the concept of the wheelbase preview control scheme, this paper selects an FxLMS algorithm as an adaptive feedforward controller when reducing $\omega_{y,\mathrm{SPM}}$ [27,28]. Figure 5 shows the block diagram of the FxLMS algorithm where $x(n)$, $e(n)$ and $u(n)$ are the reference, error and control signals, respectively. The control signal, $u(n)$, represents the vertical force generated in S_r, i.e., u_r. In Figure 5, $P(z)$ and $S(z)$ are the primary and secondary paths, respectively.

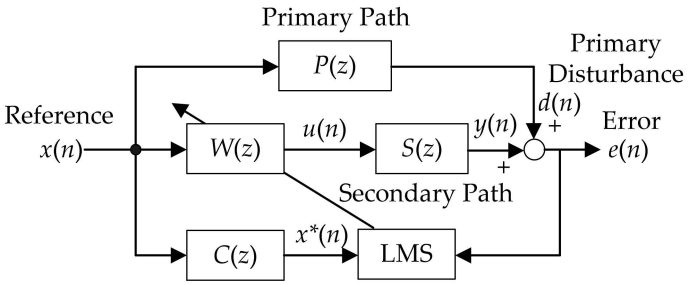


Figure 5. Block diagram of FxLMS algorithm.

For FxLMS, this paper selects $a_{z,\mathrm{SPMFC}}$ as a reference signal because it can be easily measured with A_{sf}, as shown in Figure 2. For motion sickness mitigation, $\omega_{y,\mathrm{SPM}}$ is selected as an error, $e(n)$. As a result, FxLMS tries to reduce $\omega_{y,\mathrm{SPM}}$ while LQ SOF controllers try to reduce $a_{z,\mathrm{SPM}}$.

As shown in Figure 2, u_f and u_r of LQ SOF controllers are applied to S_f and S_r, respectively. On the other hand, $u(n)$ of the FxLMS is applied to S_r. Consequently, the control input u_r of LQ SOF controllers and $u(n)$ of FxLMS are summed and applied to S_r.

For FxLMS, the secondary path, $S(z)$, should be modeled by a FIR filter, $C(z)$, which is tuned by LMS algorithm. As a result, the estimate of the secondary path, $C(z)$, is obtained and used for FxLMS, as shown in Figure 4. In FxLMS, the filter coefficients, $W(z)$, i.e., $\mathbf{w}(n)$, is updated by the LMS update rule, as given in (21) [27,28]. In (21), μ is the learning rate.

$$\mathbf{w}(n+1) = \mathbf{w}(n) - \mu e(n) x^*(n) \tag{21}$$

3. Simulation and Discussion

To validate the LQ SOF controllers and FxLMS in terms of ride comfort and motion sickness, a frequency response analysis is performed and a simulation is conducted on MATLAB/Simulink, connected to the vehicle simulation package, CarSim.

3.1. Simulation Environment

The LQ SOF controllers, FxLMS algorithm and HBM were implemented in MATLAB/Simulink. The vehicle model used for the simulation is the E-class sedan one given in CarSim [44]. For the LQ SOF controller design, the parameters of the HCM are given in Table 1 [10–12]. The parameters of the HBM were taken from the references [14–18]. ζ_i in the LQ cost functions are given in Table 2. In Table 2, ζ_8 is set to 2.0. If this value is set to a lower value than 2.0, this can cause chattering in the responses. The actuators in S_f and S_r were modeled with the first-order system with the bandwidth of 10 Hz. It is also assumed that there are no limitations on the maximum force of the actuators.

Table 1. Parameters and values of the HCM referred to from the E-class sedan model in CarSim.

Parameter	Value	Parameter	Value
m_s	1653 kg	m_u	22.5 kg
I_y	2765 kg·m^2	k_{tf}, k_{tr}	230,000 N/m
l_f	1.402 m	l_r	1.646 m
k_{sf}, k_{sr}	34,000 N/m	b_{sf}, b_{sr}	3500 Ns/m

Table 2. MAVs in LQ cost function.

ζ_1	1.0 m/s^2	ζ_2	30.0 deg/s^2	ζ_3	2.0 deg/s	ζ_4	2.0 deg
ζ_5	0.05 m	ζ_6	0.05 m	ζ_7	10,000.0 N	ζ_8	2.0 m/s^2

As a road file for the simulation in CarSim, the bounce sine sweep road (BSSR) was selected. The BSSR, given in CarSim, is shown in Figure 6, which is a sinusoidal bump with

a decreasing wavelength and amplitude over time. The vehicle speed was set to 10 m/s or 36 km/h for the simulation on the BSSR.

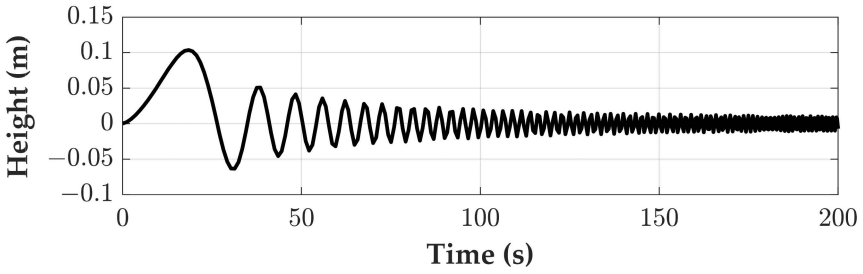


Figure 6. Bounce sine sweep road profile.

3.2. Gains of LQ SOF Controllers

LQ SOF controllers were obtained by CMA-ES from the state-space equations of HCM and HCHBM with LQ cost functions, (11) and (12). Tables 3 and 4 show the gain matrices of LQSOF.HCM and LQSOF.HCHBM, respectively.

Table 3. Gain matrices of the LQ SOF controllers designed with the HCM.

Controller	J_H	Gain Matrix
LQR	2169.7	$\mathbf{K}_{LQRH} = \begin{bmatrix} -8829 & 25124 & 27736 & -197 & 2891 & -10025 & 3066 & -110 \\ -12081 & -29243 & -322 & 28322 & 2008 & 9476 & -110 & 3119 \end{bmatrix}$
LQSOFH	2270.0	$\mathbf{K}_{SOF} = \begin{bmatrix} -6238 & -171 & 2946 & -113 & -10993 & 9067 \\ -11827 & -8825 & -114 & 2996 & 9677 & -6005 \end{bmatrix}$
LQSSOFH1	2276.8	$\mathbf{K}_{SSOF1} = \begin{bmatrix} -8378 & 31097 & 3015 & 0 & 0 & 0 \\ -8378 & -31097 & 0 & 3015 & 0 & 0 \end{bmatrix}$
LQSSOFH2	3191.2	$\mathbf{K}_{SSOF2} = \begin{bmatrix} -6350 & 28763 & 0 & 0 & 0 & 0 \\ -6350 & -28763 & 0 & 0 & 0 & 0 \end{bmatrix}$
LQSSOFH3	3190.5	$\mathbf{K}_{SSOF3} = \begin{bmatrix} 0 & 0 & 0 & 0 & -12609 & 6254 \\ 0 & 0 & 0 & 0 & 6254 & -12609 \end{bmatrix}$

Table 4. Gain matrices of the LQ SOF controllers for the HCHBM.

Controller	J_F	Gain Matrix
LQR	26,472.3	$\mathbf{K}_{LQRF}$
LQSOFH	27,008.1	$\mathbf{K}_{SOF} = \begin{bmatrix} -7391 & 4285 & 2990 & -94 & -12338 & 6795 \\ -3433 & -1630 & -86 & 3006 & 4986 & -13038 \end{bmatrix}$
LQSSOFH1	27,014.1	$\mathbf{K}_{SSOF1} = \begin{bmatrix} -12410 & 31304 & 3031 & 0 & 0 & 0 \\ -12410 & -31304 & 0 & 3031 & 0 & 0 \end{bmatrix}$
LQSSOFH2	27,992.9	$\mathbf{K}_{SSOF2} = \begin{bmatrix} -12259 & 29287 & 0 & 0 & 0 & 0 \\ -12259 & -29287 & 0 & 0 & 0 & 0 \end{bmatrix}$
LQSSOFH3	27,996.9	$\mathbf{K}_{SSOF3} = \begin{bmatrix} 0 & 0 & 0 & 0 & -15720 & 3575 \\ 0 & 0 & 0 & 0 & 3575 & -15720 \end{bmatrix}$

As shown in Table 3, the values of J_H of the SOF and structure SOF controllers, i.e., LQSOFH and LQSSOFH1, and LQSOFH2 and LQSSOFH3 have almost the same as each other. Similarly, as shown in Table 4, the values of J_F of the SOF and structure SOF controllers, i.e., LQSOFF and LQSSOFF1, and LQSOFF2 and LQSSOFF3 are nearly identical to each other. From those results, it is expected that the controllers with nearly identical J_H or J_F will show the same performance.

As shown in the tables, in terms of J_H and J_F, LQSSOFH2 and LQSSOFH3, and LQSSOFF2 and LQSSOFF3 have nearly identical values as each other for HCM and HCHBM, respectively. These facts mean that LQ SOF controller with $v_{z,\mathrm{SPM}}$ and $\omega_{y,\mathrm{SPM}}$ is equivalent to that with $v_{z,\mathrm{SPMFC}}$ and $v_{z,\mathrm{SPMRC}}$. As shown in (5), the elements, $v_{z,\mathrm{SPM}}$ and $\omega_{y,\mathrm{SPM}}$, of the vector $\mathbf{p}$ can be converted into the elements, $v_{z,\mathrm{SPM}}$ and $\omega_{y,\mathrm{SPM}}$, of the vector $\mathbf{z}_s$, and

vice versa. However, $\mathbf{K}_{SSOF3}$ is preferred to $\mathbf{K}_{SSOF2}$ because the former needs $v_{z,\mathrm{SPMFC}}$ and $v_{z,\mathrm{SPMRC}}$ and does not need the conversion of (5).

From (16), the gain group (k_1,k_2,k_7,k_8) corresponds to $v_{z,\mathrm{SPM}}$ and $\omega_{y,\mathrm{SPM}}$ and (k_5,k_6,k_{11},k_{12}) corresponds to $v_{z,\mathrm{SPMFC}}$ and $v_{z,\mathrm{SPMRC}}$. In view of the above fact, one of the gain group (k_1,k_2,k_7,k_8) or (k_5,k_6,k_{11},k_{12}) is negligible in $\mathbf{K}_{SOF}$. If one of two groups is omitted, no matter which is neglected, it is expected that the performance of the obtained controller is nearly the same.

In Tables 3 and 4, the gain elements k_4 and k_9 of $\mathbf{K}_{SOF}$ are quite small, compared to the others. This means that $v_{z,\mathrm{SSF}}$ and $v_{z,\mathrm{SSR}}$ contributes only to u_f and u_r, respectively. Based on this fact, $\mathbf{K}_{SSOF1}$ is proposed from $\mathbf{K}_{SOF}$. In view of the values of J, $\mathbf{K}_{SOF}$ and $\mathbf{K}_{SSOF1}$ are superior to $\mathbf{K}_{SSOF2}$ and $\mathbf{K}_{SSOF3}$. The advantage of using the latter is that $\mathbf{K}_{SSOF2}$ and $\mathbf{K}_{SSOF3}$ do not need $v_{z,\mathrm{SSF}}$ and $v_{z,\mathrm{SSR}}$. On the other hand, if $v_{z,\mathrm{SSF}}$ and $v_{z,\mathrm{SSR}}$ can be measured or estimated exactly, the control performance can be improved by $\mathbf{K}_{SSOF1}$, compared to $\mathbf{K}_{SSOF2}$ and $\mathbf{K}_{SSOF3}$.

3.3. Frequency Response Analysis on SOF Controllers

With the LQSOF.HCM and LQSOF.HCHBM and the state-space equations of the HCM and HCHBM, the frequency responses were drawn from z_{rf} to $a_{z,\mathrm{HEAD}}$, $a_{z,\mathrm{SPM}}$ and $\omega_{y,\mathrm{SPM}}$. Figures 7 and 8 show the frequency responses of the LQSOF.HCM and LQSOF.HCHBM, respectively.

As expected in Tables 3 and 4, the LQSSOFH2 and LQSSOFH3 and the LQSSOFF2 and LQSSOFF3 are almost the same as each other in the LQSOF.HCM and LQSOF.HCHBM, respectively. Moreover, the LQSOFH and LQSSOFH1 and the LQSOFF and LQSSOFF1 are nearly identical to each other in the LQSOF.HCM and LQSOF.HCHBM, respectively. From the above results, $\mathbf{K}_{SSOF1}$ and $\mathbf{K}_{SSOF3}$ are selected for the simulation on CarSim.

As shown in Figures 7 and 8, $\mathbf{K}_{SSOF1}$ is better than $\mathbf{K}_{SSOF3}$, which is expected from Tables 3 and 4. There are slight differences among LQSOF.HCM and LQSOF.HCHBM. More specifically, the latter shows slightly better performance in reducing $a_{z,\mathrm{HEAD}}$, $a_{z,\mathrm{SPM}}$ and $\omega_{y,\mathrm{SPM}}$ over the range below 1 Hz. This is caused by the fact that the weight ζ_8 on $a_{z.\mathrm{HEAD}}$ is large, as given in Table 2. As a result, a large ζ_8 has slight effects on the control performance. On the other hand, if ζ_8 becomes smaller, e.g., 2.0, it can cause chattering in the time responses of $a_{z.\mathrm{SPM}}$ and $a_{z.\mathrm{HEAD}}$ due to higher gain.

3.4. Simulation with LQ SOF Controllers on Bounce Sine Sweep Road

With the LQ SOF controllers, the simulation is performed on the BSSR in CarSim for comparison among those controllers. As mentioned earlier, $\mathbf{K}_{SSOF1}$ and $\mathbf{K}_{SSOF3}$ were selected for the simulation in CarSim. Figures 9 and 10 show the simulation results of $\mathbf{K}_{SSOF1}$ and $\mathbf{K}_{SSOF3}$ in LQSOF.HCM and LQSOF.HCHBM on the BSSR. Table 5 shows the peak values obtained from the simulation results shown in Figures 9 and 10. In Table 5, all the peak values were obtained over the range from 1 s to 9 s because the peaks are in the range.

Table 5. Summary of the peak values of $\mathbf{K}_{SSOF1}$ and $\mathbf{K}_{SSOF3}$ on the BSSR.

Model	Controller	$a_{z.\mathrm{SPM}}$ (m/s^2)	$a_{z.\mathrm{HEAD}}$ (m/s^2)	$\omega_{y.\mathrm{SPM}}$ (deg/s)	Max Front F. (N)	Max Rear F. (N)
	No Control	14.2	34.2	34.8		
HCM	LQSSOFH1	2.6	4.5	5.5	5498	3049
	LQSSOFH3	3.3	6.4	6.4	4035	2533
HCHBM	LQSSOFF1	2.1	4.1	5.9	6581	4098
	LQSSOFF3	2.3	5.6	6.2	5137	3582

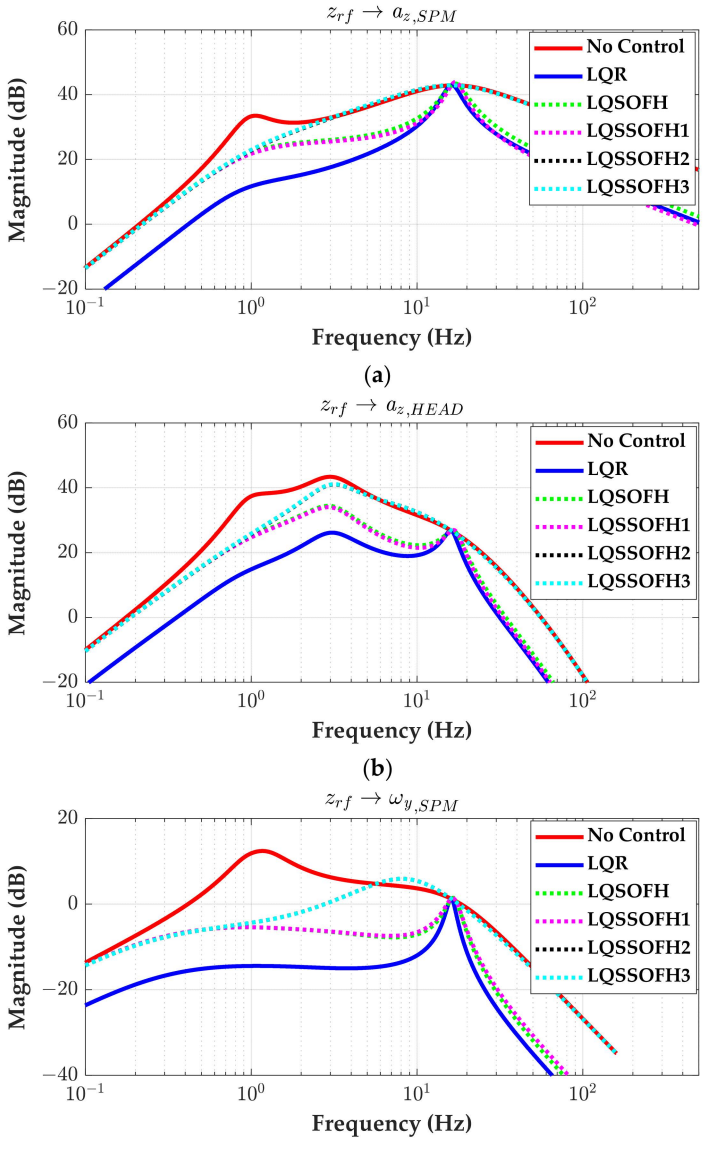


Figure 7. Frequency responses of the LQ SOF controllers designed with the HCM. (**a**) a_z of the SPM; (**b**) a_z of human head; and (**c**) ω_y of the SPM.

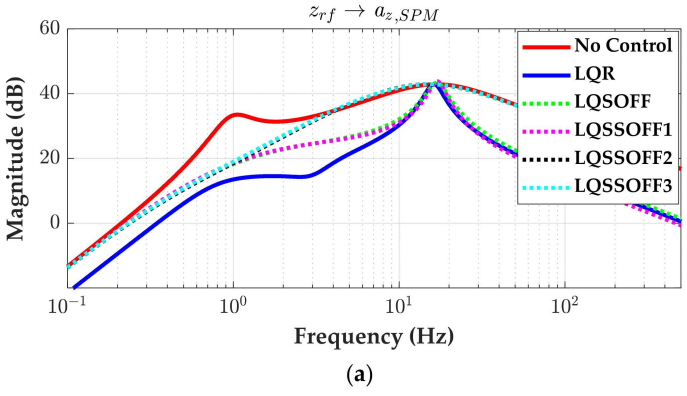


Figure 8. *Cont.*

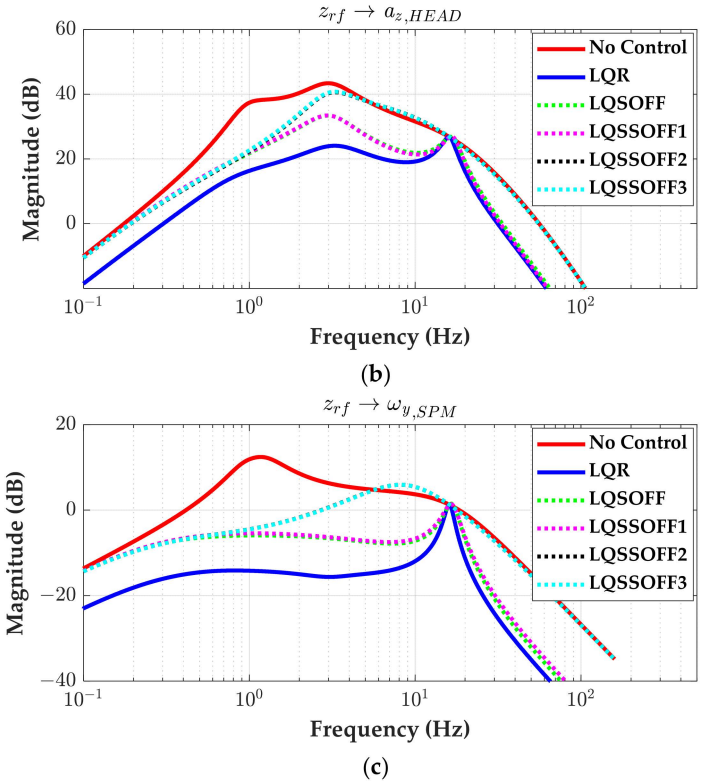


Figure 8. Frequency responses of the LQ SOF controllers designed with the HCHBM. (**a**) a_z of the SPM; (**b**) a_z of human head; and (**c**) ω_y of the SPM.

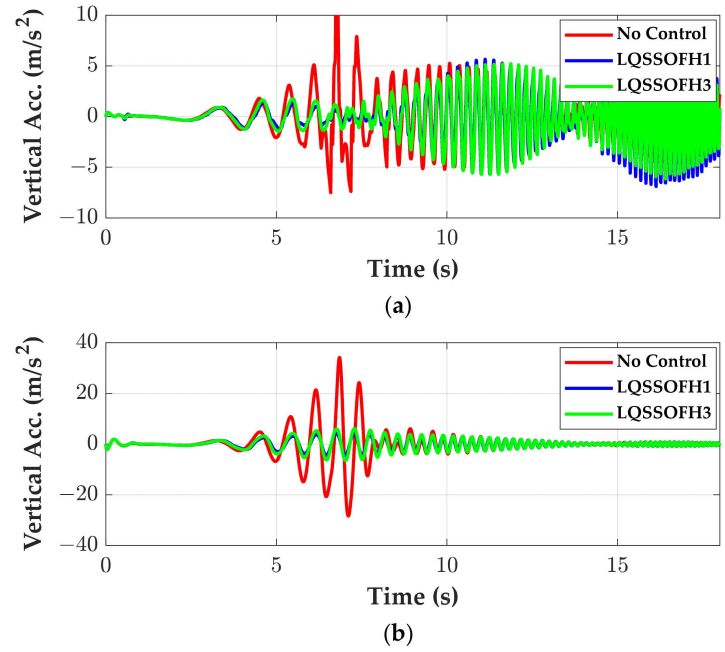


Figure 9. *Cont.*

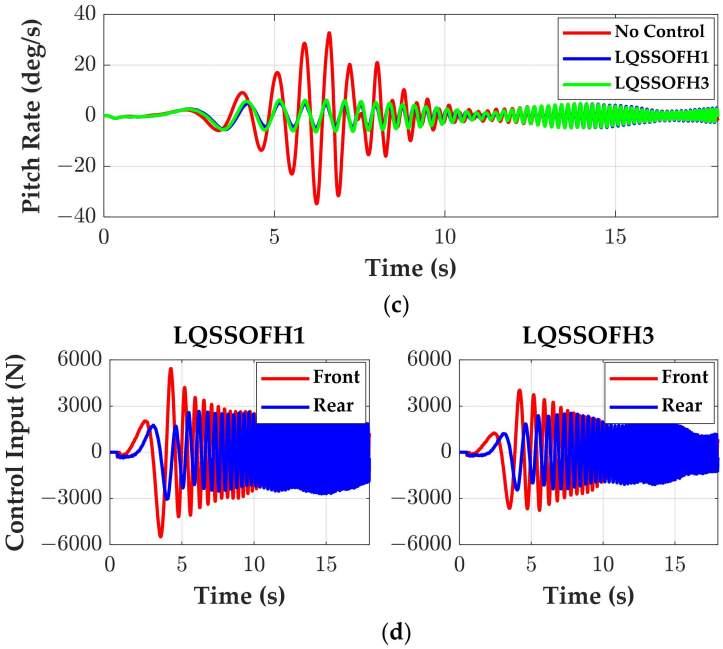


Figure 9. Simulation results of LQ SOF controllers designed with HCM on the BSSR. (**a**) a_z of SPM; (**b**) a_z of human head; (**c**) pitch rates of SPM; and (**d**) control inputs.

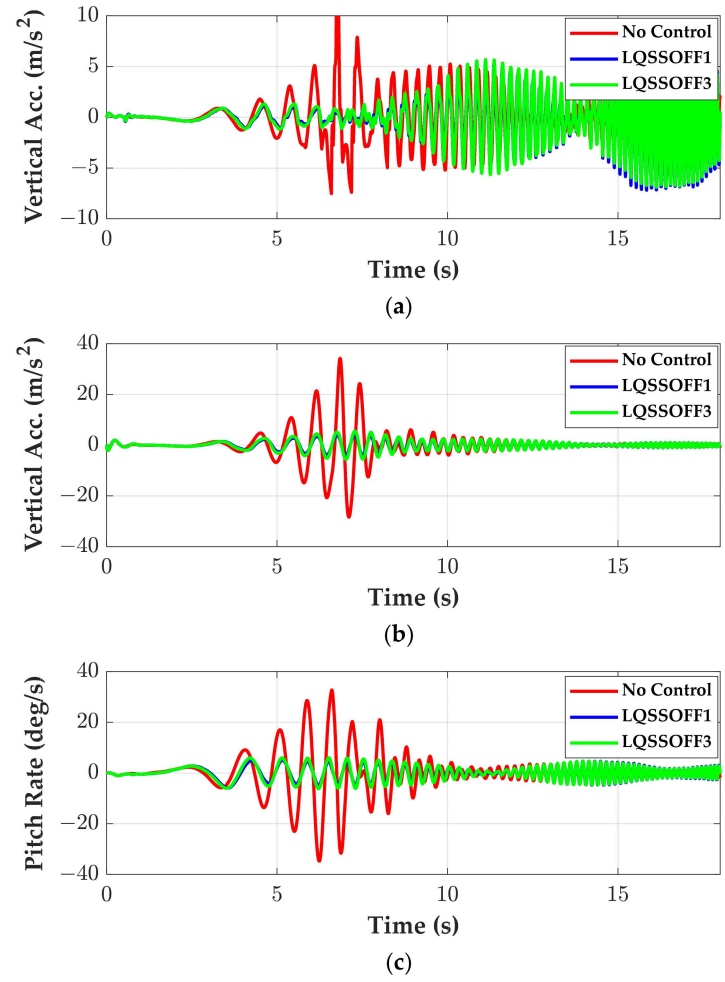


Figure 10. *Cont.*

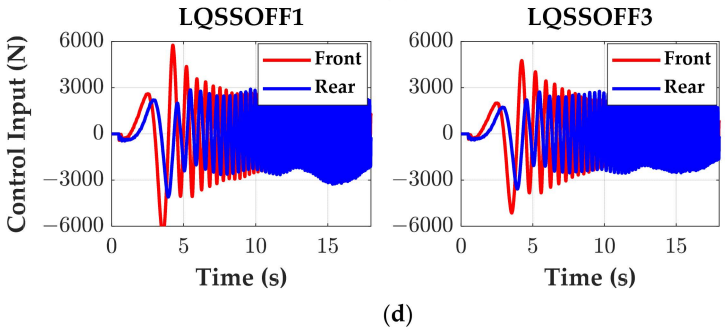


Figure 10. Simulation results of LQ SOF controllers designed with HCHBM on the BSSR. (**a**) a_z of SPM; (**b**) a_z of human head; (**c**) pitch rates of SPM; and (**d**) control inputs.

As shown in these figures, $\mathbf{K}_{SSOF1}$ and $\mathbf{K}_{SSOF3}$ greatly reduced $a_{z.\mathrm{SPM}}$, $a_{z.\mathrm{HEAD}}$ and $\omega_{y.\mathrm{SPM}}$. Especially, $a_{z.\mathrm{HEAD}}$ and $\omega_{y.\mathrm{SPM}}$ are significantly reduced over the entire frequency range of the BSSR. $\mathbf{K}_{SSOF1}$ is better than $\mathbf{K}_{SSOF3}$, which is expected from Tables 3 and 4 and Figures 7 and 8. Moreover, as shown in Table 5, the controllers in LQSOF.HCHBM are slightly better than those in LQSOF.HCM. The difference between them is that the term related to $a_{z.\mathrm{HEAD}}$ was added into the J_H of the HCM. This makes LQSOF.HCHBM slightly better than LQSOF.HCM.

From those results, it is shown that LQSOF.HCM itself is very effective in reducing $a_{z.\mathrm{HEAD}}$ and that LQSOF.HCHBM can improve the performance of LQSOF.HCM. For better performance, it is recommended that the term $a_{z.\mathrm{HEAD}}$ should be included in the LQ cost function.

Figures 9 and 10 show that there are slight differences between $\mathbf{K}_{SSOF1}$ and $\mathbf{K}_{SSOF3}$ as shown in Table 5. This is not expected from the frequency responses given in Figures 7 and 8. This fact is caused by the fact that the bandwidth of the actuators was limited to 10 Hz.

3.5. Simulation with LQ SOF Controllers and FxLMS on Bounce Sine Sweep Road

In this subsection, with the LQ SOF controller, $\mathbf{K}_{SSOF3}$, and FxLMS, the simulation is performed on CarSim. $\mathbf{K}_{SSOF3}$ was selected because it requires only two sensor signals. Figures 11 and 12 show the simulation results of the FxLMS, $\mathbf{K}_{SSOF3}$, $\mathbf{K}_{SSOF3}$+FxLMS, where $\mathbf{K}_{SSOF3}$ was selected from LQSOF.HCM and LQSOF.HCHBM. Table 6 shows the peak values obtained from the simulation results shown in Figures 11 and 12.

Table 6. Summary of the peak values of the LQ SOF controllers on the BSSR.

Model	Controller	$a_{z.SPM}$ (m/s^2)	$a_{z.HEAD}$ (m/s^2)	$\omega_{y.SPM}$ (deg/s)	Max Front F. (N)	Max Rear F. (N)
	No Control	14.2	34.2	34.8		
	FxLMS	15.3	31.8	9.0	0	9174
HCM	LQSSOFH3	3.3	6.4	6.4	4035	2533
	LQSSOFH3+FxLMS	3.4	8.6	3.8	3275	6420
HCHBM	LQSSOFF3	2.3	5.6	6.2	5137	3582
	LQSSOFF3+FxLMS	2.9	6.2	3.7	4720	4948

Figures 11 and 12 and Table 6 show that LQSOF.HCM itself is very effective in reducing $a_{z.\mathrm{SPM}}$, $a_{z.\mathrm{HEAD}}$ and $\omega_{y.\mathrm{SPM}}$ and that the FxLMS reduced only $\omega_{y.\mathrm{SPM}}$ [12]. In other words, $\omega_{y.\mathrm{SPM}}$ can be reduced further by applying the FxLMS with $\mathbf{K}_{SSOF3}$. As mentioned in the previous subsection, LQSOF.HCHBM improved the performance of LQSOF.HCM. For better performance, it is recommended that the term $a_{z.\mathrm{HEAD}}$ should be included in the LQ cost function. However, if the FxLMS is applied with the LQ SOF controllers, $a_{z.\mathrm{SPM}}$, $a_{z.\mathrm{HEAD}}$ and $\omega_{y.\mathrm{SPM}}$ are slightly increased.

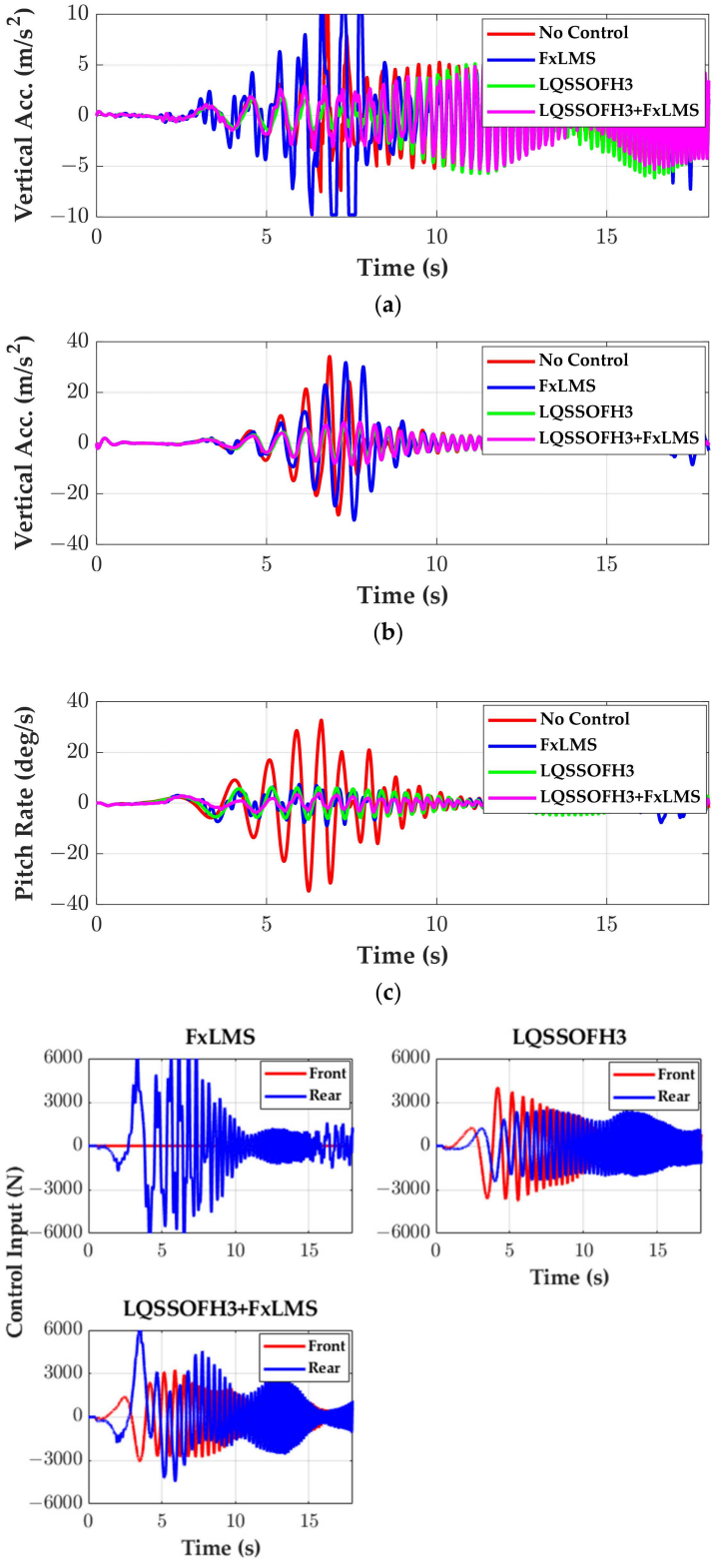


Figure 11. Simulation results of LQSSOFH3 and FxLMS on the BSSR. (**a**) a_z of SPM; (**b**) a_z of human head; (**c**) pitch rates of SPM; and (**d**) control inputs.

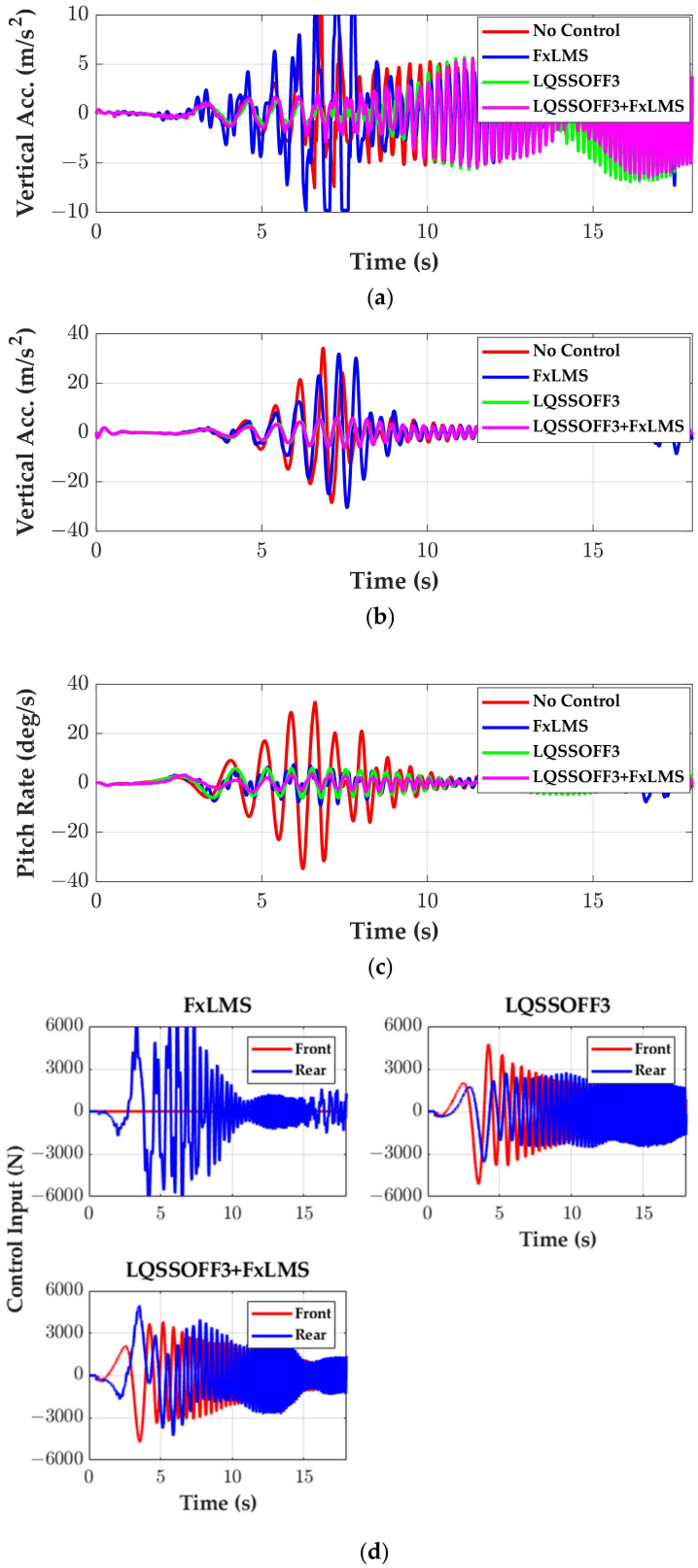


Figure 12. Simulation results of LQSSOFF3 and FxLMS on the BSSR. (**a**) a_z of SPM; (**b**) a_z of human head; (**c**) pitch rates of SPM; and (**d**) control inputs.

Figures 13 and 14 show the frequency response plots of the simulation results given in Figures 11 and 12. As shown in Figures 13 and 14, $a_{z.\mathrm{SPM}}$, $a_{z.\mathrm{HEAD}}$ and $\omega_{y.\mathrm{SPM}}$ were reduced within the frequency range from 0.1 to 3 Hz by the LQ SOF controllers and its

combination with the FxLMS. These results mean that motion sickness is mitigated within the frequency range defined in ISO2631-1. Moreover, the FxLMS is effective only when reducing $\omega_{y.\mathrm{SPM}}$. In other words, the FxLMS has little influence on reducing $a_{z.\mathrm{SPM}}$ and $a_{z.\mathrm{HEAD}}$. As discussed in the previous subsections, there are slight differences between LQSOF.HCM and LQSOF.HCHBM.

3.6. Discussions on Implementation and Realizability of the Proposed Controllers in a Real Vehicle

As shown in Figures 9–12, the maximum forces of the active actuators used for the simulation vary from 4000 N to 6000 N. The bandwidth of the active actuator was set to 10 Hz. In real vehicles, it is nearly impossible to implement the active actuator with the maximum force of 6000 N and the bandwidth of 10 Hz. For this reason, this research is to be regarded as a baseline on suspension controller design for ride comfort improvement and motion sickness mitigation. Moreover, the results obtained from this paper can be used to design a suspension controller with a semi-active suspension or a variable damper that can be realizable in real vehicles.

Recently developed magneto-rheological (MR) dampers can be used as a realistic actuator for suspension control for ride comfort improvement and motion sickness mitigation [45–48]. Figure 15 shows the damping forces of an MR damper with respect to the suspension velocity and applied current [46]. As shown in Figure 15, the MR damper has enough damping force to be used for vehicle suspension control. The size of this MR damper is small enough to be installed in a real vehicle. Moreover, the commercial MR damper, developed by Lord Corporation, can reduce the vertical acceleration of the sprung mass within the range from 0 to 10 Hz [45]. From these facts, the MR damper can be used for suspension control. In future work, the proposed algorithm will be tested on a real vehicle equipped with an MR damper. Different from the active actuator, the control performance will be deteriorated due to the semi-active nature of the MR damper.

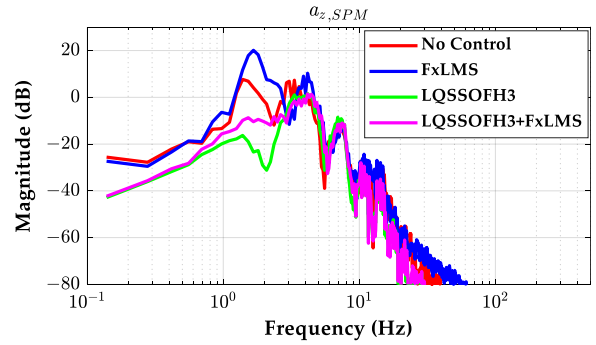
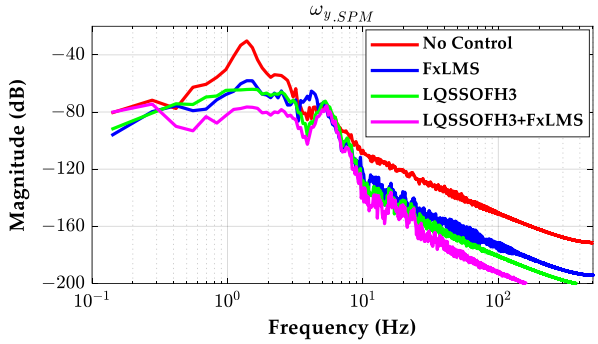
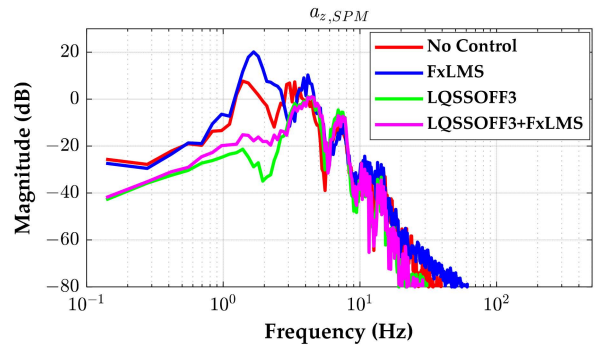


Figure 13. *Cont.*

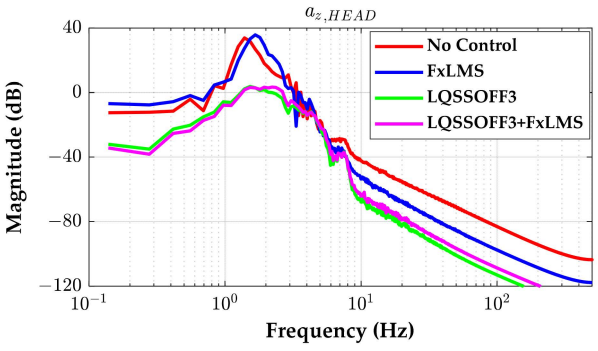


(**c**)

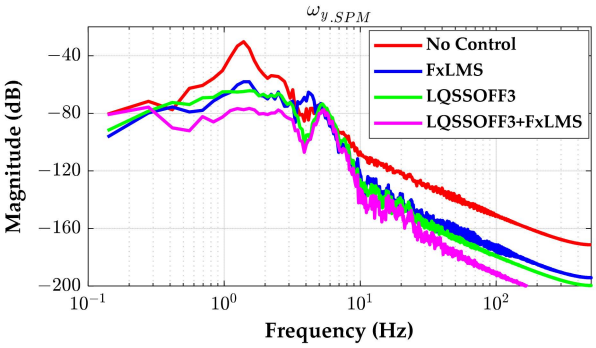
Figure 13. Frequency responses of LQSOFH4 and FxLMS controllers. (**a**) a_z of SPM; (**b**) a_z of human head; and (**c**) pitch rates of SPM.



(**a**)



(**b**)



(**c**)

Figure 14. Frequency responses of LQSOFF4 and FxLMS controllers. (**a**) a_z of SPM; (**b**) a_z of human head; and (**c**) pitch rates of SPM.

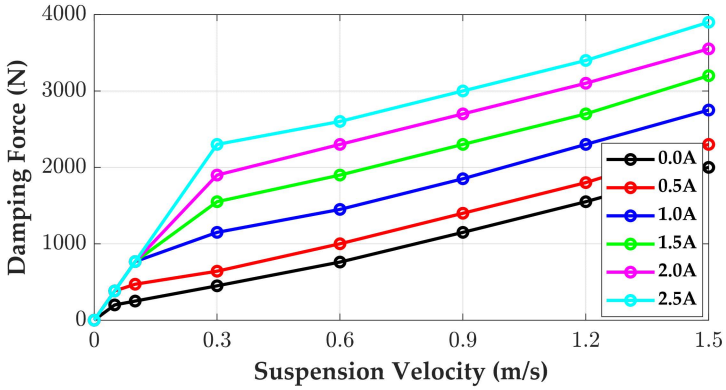


Figure 15. Damping force of an MR damper used for suspension control [46].

4. Conclusions

This paper presented a method to design a suspension controller with a human body model for the purpose of reducing motion sickness. For the controller design, the half-car and human body models (HCM and HCHBM) were adopted. Using these models, the corresponding state-space equations were derived. To be implemented in real vehicles, three types of structured SOF controllers were proposed. For the SOF controllers, six signals were selected as an output. The LQ cost functions were defined for the HCM and HCHBM. With the LQ cost functions and state-space equations for the HCM and HCHBM, LQ SOF controllers were designed. To reduce the pitch rate of the sprung mass, the FxLMS was designed and applied with the LQ SOF controllers.

To verify the performance of the LQ SOF controllers and FxLMS, a frequency response analysis was performed and a simulation was conducted on vehicle simulation software, CarSim. From the simulation results, the following conclusions were drawn:

- Among the LQ SOF controllers, it was shown that $\mathbf{K}_{SOF}$ and $\mathbf{K}_{SSOF1}$, and $\mathbf{K}_{SSOF2}$ and $\mathbf{K}_{SSOF3}$, are equivalent to each other, respectively. If the suspension velocities at the front/rear corners of the sprung mass are selected as an output for the SOF controller, it makes the difference between the two groups.
- The LQ SOF controller designed with the HCM (LQSOF.HCM) can effectively reduce the vertical acceleration of a human head. If the LQ SOF controller is designed with the HCHBM, it can improve performance over LQSOF.HCM. For better performance, it is recommended that the LQ SOF controller should be designed with the HCHBM.
- The FxLMS can reduce only the pitch rate of the sprung mass. Instead, performance of the LQ SOF controllers is slightly deteriorated in terms of the vertical acceleration of the SPM.

To sum up, the proposed LQ SOF controllers and FxLMS are effective for ride comfort improvement and motion sickness mitigation in that the combined controller can reduce the vertical acceleration and the pitch rate of the sprung mass within the range of 0.8~8 Hz. Moreover, the LQ SOF controllers can reduce the vertical acceleration and the pitch rate within the frequency range of 0.2~3 Hz, which satisfies the motion sickness mitigation defined in ISO2631-1.

As given in the simulation results, the maximum actuator force of the active actuator is too large to be realized in real vehicles. Moreover, a high bandwidth over 10 Hz is required for good performance. However, it is nearly impossible to implement this type of active actuator in real vehicles. Instead of the active actuator, semi-active actuators such as a variable damper or an MR damper, which can be implemented in real vehicles, can be used as an actuator for suspension control in future research. For that purpose, this research can be used as a baseline.

Author Contributions: Conceptualization, S.Y.; methodology, S.Y.; software, J.K. and S.Y.; validation, J.K. and S.Y.; formal analysis, S.Y.; investigation, J.K. and S.Y.; resources, S.Y.; data curation, J.K. and S.Y.; writing—original draft preparation, J.K. and S.Y.; writing—review and editing, J.K.; visualization, J.K.; supervision, S.Y.; funding acquisition, S.Y. All authors have read and agreed to the published version of the manuscript.

Funding: This research received no external funding.

Data Availability Statement: The original contributions presented in this study are included in the article; further inquiries can be directed to the corresponding author/s.

Acknowledgments: This study was supported by the Research Program funded by Seoul National University of Science and Technology.

Conflicts of Interest: The authors declare no conflicts of interest.

Nomenclature

A_{sf}, A_{sr}	accelerometers attached on the front/rear corners of a sprung mass
A_{uf}, A_{ur}	accelerometers attached on the front/rear wheel centers
HCM	half-car model
HBM	human body model
HCHBM	combined half-car and human body models
LQR	linear quadratic regulator
LQSOF	linear quadratic static output feedback
LQSSOF	linear quadratic structured static output feedback
SOF	static output feedback
SPM	sprung mass or vehicle body
SPMFC	front corner of sprung mass
SPMRC	rear corner of sprung mass
SSF, S_f	front suspension
SSR, S_r	rear suspension
SSE	state-space equation
SSOF	structured static output feedback
WBPCS	wheelbase preview control scheme
a, b	distances from center of gravity of a sprung mass to front/rear corners (m)
a_z	vertical or heave acceleration (m/s^2)
$a_{z,HEAD}$	vertical or heave acceleration of a human head (m/s^2)
$a_{z,SPM}$	vertical or heave acceleration of a sprung mass (m/s^2)
$a_{z,SPMFC}$	vertical or heave acceleration at front corner of a sprung mass (m/s^2)
$a_{z,SPMRC}$	vertical or heave acceleration of rear corner of a sprung mass (m/s^2)
$a_{z,USPM}$	vertical or heave acceleration of an unsprung mass (m/s^2)
b_i	damping coefficient of a human body component (N·s/m)
b_{sf}, b_{sr}	damping coefficient of a damper at front/rear suspensions (N·s/m)
I_y	pitch moment of inertia (kg·m^2)
J_H, J_F	LQ cost function used for LQ controllers from HCM and HCHBM
k_i	stiffness of a human body component (N/m)
k_{sf}, k_{sr}	stiffness of a spring at front/rear suspensions (N/m)
k_{tf}, k_{tr}	stiffness of front/rear tires (N/m)
m_s	sprung mass (kg)
m_{uf}, m_{ur}	unsprung mass under front/rear suspensions (kg)
u_f, u_r	forces generated by an actuator at front/rear suspensions (N)
v_z	vertical velocity (m/s)
$v_{z,SPM}$	vertical or heave velocity of a sprung mass (m/s)
$v_{z,SSF}$	suspension velocity of front suspension (m/s)
$v_{z,SSR}$	suspension velocity of rear suspension (m/s)
$v_{z,USPM}$	vertical or heave velocity of an unsprung mass (m/s)
z_c	heave displacement at center of gravity of a sprung mass (m)
z_{rf}, z_{rr}	road elevation acting on front/rear tires (m)
z_{sf}, z_{sr}	vertical displacement of front/rear corners of a sprung mass (m)

z_{uf}, z_{ur}	vertical displacement of front/rear wheel centers (m)
ξ_i	maximum allowable value (MAV) of weight in LQ cost function
$\omega_{y,SPM}$	pitch rate of a sprung mass (rad/s)
ρ_i	weight in LQ cost function
θ	pitch angle of a sprung mass (rad)

References

1. Tseng, H.E.; Hrovat, D. State of the art survey: Active and semi-active suspension control. *Veh. Syst. Dyn.* **2015**, *53*, 1034–1062. [CrossRef]
2. Wilson, D.A.; Sharp, R.S.; Hassan, S.A. The application of linear optimal control theory to the design of active automobile suspensions. *Veh. Syst. Dyn.* **1987**, *15*, 105–118. [CrossRef]
3. Cao, D.; Song, X.; Ahmadian, M. Editors' perspectives: Road vehicle suspension design, dynamics, and control. *Veh. Syst. Dyn.* **2011**, *49*, 3–28. [CrossRef]
4. *ISO 2631-1*; Mechanical Vibration and Shock—Evaluation of Human Exposure to Whole-Body Vibration—Part 1: General Requirements. International Organization for Standardization: Geneva, Switzerland, 1997.
5. Diels, C.; Bos, J.E. Self-driving carsickness. *Appl. Ergon.* **2016**, *53*, 374–382. [CrossRef]
6. Dam, A.; Jeon, M. A review of motion sickness in automated vehicles. In Proceedings of the 13th International Conference on Automotive User Interfaces and Interactive Vehicular Applications, Leeds, UK, 9–14 September 2021; pp. 39–48.
7. Ekchian, J.; Graves, W.; Anderson, Z.; Giovanardi, M.; Godwin, O.; Kaplan, J.; Ventura, J.; Lackner, J.R.; DiZio, P. *A High-Bandwidth Active Suspension for Motion Sickness Mitigation in Autonomous Vehicles*; SAE Technical Paper 2016-01-1555; SAE International: Warrendale, PA, USA, 2016.
8. DiZio, P.; Ekchian, J.; Kaplan, J.; Ventura, J.; Graves, W.; Giovanardi, M.; Anderson, Z.; Lackner, J.R. An active suspension system for mitigating motion sickness and enabling reading in a car. *Aerosp. Med. Hum. Perform.* **2018**, *89*, 822–829. [CrossRef]
9. Jurisch, M.; Holzapfel, C.; Buck, C. The influence of active suspension systems on motion sickness of vehicle occupants. In Proceedings of the IEEE 23rd International Conference on Intelligent Transportation Systems, Rhodes, Greece, 20–23 September 2020.
10. Jeong, Y.; Yim, S. Design of active suspension controller for ride comfort enhancement and motion sickness mitigation. *Machines* **2024**, *12*, 254. [CrossRef]
11. Kim, J.; Yim, S. Design of static output feedback suspension controllers for ride comfort improvement and motion sickness reduction. *Processes* **2024**, *12*, 968. [CrossRef]
12. Kim, J.; Yim, S. Design of a suspension controller with an adaptive feedforward algorithm for ride comfort enhancement and motion sickness mitigation. *Actuators* **2024**, *13*, 315. [CrossRef]
13. Liang, C.; Chiang, C. A study on biodynamic models of seated human subjects exposed to vertical vibration. *Int. J. Ind. Ergon.* **2006**, *36*, 869–890. [CrossRef]
14. Koulocheris, D.; Papaioannou, G.; Christodoulou, D. An approach for multi-objective optimization of vehicle suspension system. *IOP Conf. Ser. Mater. Sci. Eng.* **2017**, *252*, 012037. [CrossRef]
15. Papaioannou, G.; Koulocheris, D. An approach for minimizing the number of objective functions in the optimization of vehicle suspension systems. *J. Sound Vib.* **2018**, *435*, 149–169. [CrossRef]
16. Papaioannou, G.; Voutsinas, A.; Koulocheris, D.; Antoniadis, I. Dynamic performance analysis of vehicle seats with embedded negative stiffness elements. *Veh. Syst. Dyn.* **2019**, *58*, 307–337. [CrossRef]
17. Papaioannou, G.; Sekulic, D.; Velenis, E.; Antoniadis, I. *Investigation of Seat Suspensions with Embedded Negative Stiffness Elements for Isolating Bus Users' Whole-Body Vibrations*; SAE Technical Paper 2021-01-5019; SAE International: Warrendale, PA, USA, 2021.
18. Patil, M.K.; Palanichamy, M.S.; Ghista, D.N. Dynamic response of human body seated on a tractor and effectiveness of suspension Systems. *SAE Trans.* **1977**, *86*, 3221–3235.
19. Camino, J.F.; Zampieri, D.E.; Peres, P.L.D. Design of a vehicular suspension controller by static output feedback. In Proceedings of the American Control Conference, San Diego, CA, USA, 2–4 June 1999; pp. 3168–3171.
20. Elmadany, M.M.; Al-Majed, M.I. Quadratic synthesis of active controls for a quarter-car model. *J. Vib. Control* **2001**, *7*, 1237–1252. [CrossRef]
21. Park, M.; Yim, S. Design of static output feedback and structured controllers for active suspension with quarter-car model. *Energies* **2021**, *14*, 8231. [CrossRef]
22. Jeong, Y.; Shon, Y.; Chang, S.; Yim, S. Design of static output feedback controllers for an active suspension system. *IEEE Access* **2022**, *10*, 26948–26964. [CrossRef]
23. Soliman, A.M.A.; Crolla, D.A. *Limited Bandwidth Active Suspension Employing Wheel Base Preview*; SAE Technical Paper 2001-01-1063; SAE International: Warrendale, PA, USA, 2001.
24. ElMadany, M.M.; Al Bassam, B.A.; Fayed, A.A. Preview control of slow-active suspension systems. *J. Vib. Control* **2011**, *17*, 245–258. [CrossRef]
25. Li, P.; Lam, J.; Cheung, K.C. Multi-objective control for active vehicle suspension with wheelbase preview. *J. Sound Vib.* **2014**, *333*, 5269–5282. [CrossRef]
26. Theunissen, J.; Tota, A.; Gruber, P.; Dhaens, M.; Sorniotti, A. Preview-based techniques for vehicle suspension control: A state-of-the-art review. *Annu. Rev. Control* **2021**, *51*, 206–235. [CrossRef]

27. Widrow, B.; Stearns, S.D. *Adaptive Signal Processing*; Prentice Hall, International (UK) Limited: London, UK, 1985.
28. Kuo, S.M.; Morgan, D.R. *Active Noise Control Systems-Algorithms and DSP Implementations*; Wiley: New York, NY, USA, 1996.
29. Bryson, A.E., Jr.; Ho, Y. *Applied Optimal Control*; Hemisphere: New York, NY, USA, 1975.
30. Hong, K.; Sohn, H.; Hedrick, J.K. Modified skyhook control of semi-active suspensions: A new model, gain scheduling, and hardware-in-the-loop tuning. *J. Dyn. Syst. Meas. Control* **2002**, *124*, 158–167. [CrossRef]
31. Ding, R.; Wang, R.; Meng, X.; Chen, L. Energy consumption sensitivity analysis and energy-reduction control of hybrid electromagnetic active suspension. *Mech. Syst. Signal Process.* **2019**, *134*, 106301. [CrossRef]
32. Liu, W.; Wang, R.; Ding, R.; Meng, X.; Yang, L. On-line estimation of road profile in semi-active suspension based on unsprung mass acceleration. *Mech. Syst. Signal Process.* **2020**, *135*, 106370. [CrossRef]
33. Hansen, N.; Muller, S.D.; Koumoutsakos, P. Reducing the time complexity of the derandomized evolution strategy with covariance matrix adaptation (CMA-ES). *Evol. Comput.* **2003**, *11*, 1–18. [CrossRef] [PubMed]
34. Hansen, N. The CMA evolution strategy: A comparing review. In *Towards a New Evolutionary Computation*; Advances in Estimation of Distribution Algorithms; Lozano, J.A., Larrañga, P., Inza, I., Bengoetxea, E., Eds.; Springer: Berlin/Heidelberg, Germany, 2006; pp. 75–102.
35. Kwak, B.H.; Kim, H.S.; Park, Y. Adaptive control of active suspension systems with preview. In Proceedings of the 13th Korean Automatic Control Conference (KACC), Pusan, Republic of Korea, 15–17 October 1998. (In Korean)
36. Feng, J.; Bei, S.; Yuan, C.; Zhang, L. Research on wheelbase preview control for vehicle semi-active suspension based on neural networks. In Proceedings of the 2009 Third International Symposium on Intelligent Information Technology Application, Nanchang, China, 21–22 November 2009.
37. Krauze, P.; Kasprzyk, J. FxLMS algorithm with preview for vibration control of a half-car model with magnetorheological dampers. In Proceedings of the 2014 IEEE/ASME International Conference on Advanced Intelligent Mechatronics (AIM), Besançon, France, 8–11 July 2014.
38. Strohm, J.N.; Lohmann, B. A fast convergence FxLMS algorithm for vibration damping of a quarter car. In Proceedings of the 2018 IEEE Conference on Decision and Control (CDC), Miami, FL, USA, 17–19 December 2018.
39. Krauze, P.; Kasprzyk, J. FxLMS control of an off-road vehicle model with magnetorheological dampers. In *Advanced, Contemporary Control*; Advances in Intelligent Systems and Computing; Bartoszewicz, A., Kabziński, J., Kacprzyk, J., Eds.; Springer: Cham, Switzerland, 2020; Volume 1196.
40. An, K.; Kim, D.; Kim, S.; Choi, J.; Lee, C.; Kim, H.; Lee, S.K.; Im, M.; Cho, H.S.; An, C.; et al. Active vibration control system for attenuation of structure borne road noise by tire cavity resonance using piezoelectric stack actuators. SAE Technical Paper. In Proceedings of the 13th International Styrian Noise, Vibration & Harshness Congress: The European Automotive Noise Conference, Graz, Austria, 19–21 June 2024.
41. Okda, S.; Nampally, S.R.; Fontana, M.; Herold, S.; Nordmann, R.; Rinderknecht, S.; Melz, T. Active vibration control of gearbox housing using inertial mass actuators. *Smart Mater. Struct.* **2024**, *33*, 095008. [CrossRef]
42. Jiang, J.; Gao, Z.; Zhang, H.; Zhu, X. Research on active vibration control of blade using variable-step-size filtered-x least mean square algorithm. *J. Vib. Control* **2024**. [CrossRef]
43. Wu, T.; Chen, T.; Yan, H.; Qu, J. An Improved FXLMS algorithm based on error weight for active vibration control of plates. *J. Vib. Eng. Technol.* **2024**, *12*, 3289–3303. [CrossRef]
44. Mechanical Simulation Corporation. *CarSim Data Manual*; Version 8; Mechanical Simulation Corporation: Ann Arbor, MI, USA, 2009.
45. Du, H.; Sze, K.Y.; Lam, J. Semi-active H control of vehicle suspension with magneto-rheological dampers. *J. Sound Vib.* **2005**, *283*, 981–996. [CrossRef]
46. Oh, J.S.; Choi, S.B. Ride quality control of a full vehicle suspension system featuring magnetorheological dampers with multiple orifice holes. *Front. Mater.* **2019**, *6*, 8. [CrossRef]
47. Kim, B.G.; Yoon, D.S.; Kim, G.W.; Choi, S.B.; Tan, A.S.; Sattel, T. Design of a novel magnetorheological damper adaptable to low and high stroke velocity of vehicle suspension system. *Appl. Sci.* **2020**, *10*, 5586. [CrossRef]
48. Nguyen, S.D.; Lam, B.D.; Choi, S.B. Smart dampers-based vibration control—Part 2: Fractional order sliding control for vehicle suspension system. *Mech. Syst. Signal Process.* **2021**, *148*, 107145. [CrossRef]

Disclaimer/Publisher's Note: The statements, opinions and data contained in all publications are solely those of the individual author(s) and contributor(s) and not of MDPI and/or the editor(s). MDPI and/or the editor(s) disclaim responsibility for any injury to people or property resulting from any ideas, methods, instructions or products referred to in the content.